Upwelling on the continental slope of the Alaskan Beaufort Sea: Storms, ice, and oceanographic response

Robert S. Pickart*, G.W.K. Moore†, Daniel J. Torres*, Paula S. Fratantoni*,

Roger A. Goldsmith*, Jiayan Yang*

June 2009

Accepted in Journal of Geophysical Research

---

* *Woods Hole Oceanographic Institution; Woods Hole, MA 02540 USA*

† *University of Toronto; Toronto, OT M5S 1A1 Canada*

Abstract

The characteristics of Pacific-born storms that cause upwelling along the Beaufort Sea continental slope, the oceanographic response, and the modulation of the response due to sea-ice are investigated. In fall 2002 a mooring array located near 152°W measured 11 significant upwelling events that brought warm and salty Atlantic water to shallow depths. Comparing the storms that caused these events to other Aleutian lows that did not induce upwelling, interesting trends emerged. Upwelling occurred most frequently when storms were located in a region near the eastern end of the Aleutian Island Arc and Alaskan Peninsula. Not only were these storms deep, but they generally had northward tending trajectories. While the steering flow aloft aided this northward progression, the occurrence of lee cyclogenesis due to the orography of Alaska seems to play a role as well in expanding the meridional influence of the storms. In late-fall and early-winter both the intensity and frequency of the upwelling diminished significantly at the array site. It is argued that the reduction in amplitude was due to the onset of heavy pack-ice, while the decreased frequency was due to two different upper-level atmospheric blocking patterns inhibiting the far field influence of the storms.

1 Introduction

Upwelling of warm and salty Atlantic Water onto the continental shelves of the Chukchi and Beaufort Seas in the western Arctic Ocean is commonly observed. It is particularly pronounced in the three major canyons that cut into these shelves: Barrow and Herald Canyons in the Chukchi Sea and Mackenzie Canyon in the Beaufort Sea (see Fig 1). Numerous forcing mechanisms have been put forth to explain the up-canyon flow, which at times can penetrate far onto the shelf (e.g. Bourke and Paquette, 1976). For example, Carmack and Kulikov (1998) argue that local winds drive the upwelling in Mackenzie canyon. However, velocity timeseries in Barrow canyon are

generally uncorrelated with the local wind field (Mountain et al., 1976; Aagaard and Roach, 1990). This led Mountain et al. (1976) to suggest that the meridional sea level pressure (SLP) gradient was responsible for the observed upwelling in that canyon.

There are other possible candidates for upwelling in canyons that are not directly related to the local winds. Using current meter data in Barrow Canyon, together with concurrent moored measurements along the Beaufort slope, Aagaard and Roach (1990) found a coherent, but lagged, upwelling signal at three different widely spaced sites. Consequently they suggested that the upwelling in Barrow canyon was due to a large-scale eastward-propagating shelf-edge wave. Evidence for eastward propagating waves with a displaced pycnocline was also found by Carmack and Kulikov (1998) along the Canadian Beaufort slope. A modeling study by Signorini et al. (1997) showed that rectified up-canyon flow in Barrow Canyon can occur in response to time-varying outflow of Pacific Water. Finally, Kämpf (2005) demonstrated that upwelling can occur in response to dense shelf water flowing down a canyon. While Kämpf (2005) used this result to explain velocity measurements in Orkney Passage in the Antarctic, it could apply to Barrow Canyon as well, since dense winter-transformed Pacific Water is known to cascade down the canyon (e.g. Weingartner et al., 1998; Ivanov et al., 2004; Pickart et al., 2005).

Away from canyons, upwelling has also been observed along the continental margin of the southern Canada Basin (Aagaard et al., 1981; Carmack and Kulikov, 1998; Pickart, 2004; Llinas et al., 2009; Nikolopoulos et al., 2009). Carmack and Kulikov (1998) argued that upwelling in the eastern Beaufort was driven by disturbances originating from Mackenzie Canyon that propagated eastward as a first baroclinic mode Kelvin wave. However, there is evidence that, on the Alaskan Beaufort and Chukchi continental slopes, upwelling is forced via local winds. For example, Nikolopoulos et al. (2009) showed that the dominant mode of velocity variability at 152 °W during

fall and winter was that of westward flow reversals of the boundary current due to easterly wind events. As discussed below, the associated water mass signals during these events are consistent with upwelling of Atlantic Water. This is in line with the observations of Aagaard et al. (1981) at a similar location, and with the measurements of Llinas et al. (2009) along the Chukchi slope.

From a pan-Arctic perspective, the western Beaufort and Chukchi Seas together comprise one of the two areas (the other site being near Fram Strait) where the wind-driven Ekman transport is strongest (Yang, 2006). Yang demonstrated that during the fall and winter months, offshore flow in the upper layer (driven by easterly winds) carries heat and freshwater into the Beaufort Gyre and also leads to strong upwelling along the margins of the Chukchi and Beaufort Seas. The seasonally strengthened windstress and ice motion causing the upwelling stems from the enhanced SLP gradients between the Beaufort high and Aleutian low. This is largely due to a deeper Aleutian low, since the Beaufort high is in fact strongest in March after the upwelling has largely subsided. Yang (2006) used monthly-averaged climatological fields in his analysis, and the resulting trends are consistent with the seasonal progression of the Aleutian low SLP, which reaches its minimum value in late-fall and winter (e.g. Favorite et al., 1976).

It is of course the individual Pacific-born storms that are responsible for the integrated Aleutian low signature (e.g. Terada and Hanzawa, 1984; Wilson and Overland, 1986; Gyakum et al., 1989; Zhang et al., 2004; Pickart et al., 2009a). Also, the strong easterly winds in the southern Beaufort Sea resulting from these storms likely drive the individual upwelling events seen in the mooring records from the Beaufort slope (e.g. Aagaard et al, 1981; Nikolopoulos et al., 2009). It is of interest then to understand what factors dictate the behavior and evolution of the storms that result in upwelled Atlantic Water on the shelf, and how the presence of sea-ice impacts the oceanographic response. This is the subject of the present study.

In summer 2002 a mooring array was deployed across the Alaskan Beaufort continental slope near 152°W (Fig 1), and numerous upwelling events were recorded during the subsequent fall and winter months. In this paper we use atmospheric re-analysis fields to characterize the north Pacific storms that caused the upwelling, and contrast these to the remaining low pressure systems that did not significantly influence the southern Beaufort Sea. It is found that certain features of the storms, including their upper-level steering flow and interaction with orography, are conducive for expanding their northern influence and causing strong easterly winds along the north slope of Alaska. We begin the paper with a brief overview of the circulation of the Chukchi and Beaufort Seas, followed by a description of the mooring array and the signature of upwelling seen in the hydrographic and velocity timeseries. Then we analyze the spatial patterns and tracks of the Pacific-born storms during the fall and early winter of 2002, highlighting their link to the upwelling. Finally, we discuss the role of sea-ice and upper-level atmospheric blocking patterns in modulating the occurrence and amplitude of the upwelling.

2 Data and Methods

2.1 Beaufort Slope Mooring Data and Winds

The major currents of the Chukchi and Beaufort Seas are shown schematically in Fig 1. The inflow of Pacific Water from Bering Strait splits into branches, one of which is the Alaskan Coastal Current (Paquette and Bourke, 1974; Mountain et al., 1976; Weingartner et al., 1998; Woodgate et al., 2005). Upon reaching Barrow Canyon (northern tip of Alaska), some portion of the Alaskan Coastal Current turns eastward as a shelfbreak jet (Pickart, 2004; Nikolopoulos et al., 2009). A similar eastward-flowing boundary current exists along the edge of the Chukchi Sea (Mathis et al.,

2007; Llinas et al., 2009). Presumably this is fed by the outflow from Herald Canyon (Pickart et al., 2009b), but this has not been verified (hence the gap in the schematic flow of Fig 1 to the east of Herald Canyon). It is likely that the Chukchi shelfbreak jet merges with the Alaskan Coastal Current to form a composite boundary current along the Beaufort shelfbreak/slope. Strictly speaking, the Alaskan Coastal Current is a seasonal phenomenon in the Chukchi Sea, advecting warm and fresh Alaskan Coastal Water northward in summer and fall. However, the Beaufort shelfbreak jet is present year-round, advecting both summer and winter Pacific-origin water masses to the east when the winds are weak (Nikolopoulos et al., 2009).

In summer 2002, as part of the Western Arctic Shelf-Basin Interactions program (SBI, Grebmeier and Harvey, 2005), a moored array was deployed across the Beaufort shelfbreak and slope near 152°W (Fig 2). The array consisted of moored conductivity/temperature/depth (CTD) profilers at all the sites, upward-facing acoustic Doppler current profilers (ADCPs) at the inner five moorings, and profiling acoustic current meters at the outer two moorings. This configuration produced multiple vertical sections per day of hydrographic variables and velocity. The reader is referred to Nikolopoulos et al. (2009) and Spall et al. (2008) for details about the instrumentation, measurement accuracies, and construction of the vertical sections. These studies present a basic description of the boundary current and its sensitivity to wind (Nikolopoulos et al., 2009), as well as the stability characteristics of the flow and its tendency to form eddies in the absence of wind (Spall et al, 2008).

The closest meteorological station to the mooring array is located at Pt. Barrow, AK, approximately 150 km to the west (see Fig 1). We used the edited, interpolated 10 m winds from the meteorological station as described in Nikolopoulos et al. (2009). The wind velocities were then converted to windstress following Large and Pond (1981), and the component of stress in the

direction of the northern Alaskan coastline was computed (which correlates most strongly with the mooring velocity records). Based on the analysis of Nikolopoulos et al. (2009), the measured winds at Pt. Barrow are a good proxy for the winds at the array site. The timing of storm events appears to be very similar, which is supported by the high correlation between the Pt. Barrow windstress and the ice velocity at the array site (see Section 3.3 below). There may, however, be differences in amplitude (e.g. see Nikolopoulos et al., 2009), which should be kept in mind when considering the results below.

The year-long mean vertical sections of alongstream velocity, potential temperature, and salinity for the upper 300 m are shown in Fig 3 (top panel). Note that the CTD moored profilers did not sample the upper 40-50 m of the water column due to the potential for ice ridging at these depths. Positive velocities are southeastward directed along 125°T. This is the dominant direction of the boundary current (Nikolopoulos et al., 2009). In the mean, the boundary current is bottom-intensified and trapped to the shelfbreak, flowing approximately 15 cms^{-1} to the east (with a weak "tail" extending to 250 m). The current has distinct seasonal configurations, but in the mean it advects Pacific-origin summer water near the shelfbreak (at depths shallower than 100 m) and Pacific-origin winter water at deeper depths (to roughly 150 m). Below this resides the warm (>-1.2°C) and salty (>33.6) Atlantic Water. As discussed in Nikolopoulos et al. (2009), the boundary current readily reverses to the west under easterly winds, which are common in the fall and winter. An example of this is shown in Fig 3 (bottom panel) for a storm in early November, 2002. In this case the boundary current was flowing nearly 1 ms^{-1} to the west as a surface-intensified jet. Coincident with this, the isohalines (and isopycnals) were sloped strongly upwards toward the boundary, and upwelled Atlantic water was present on the shelf.

We devised two different methods for identifying the upwelling events in the mooring records. The first approach used the gridded vertical sections extending across the entire array. For velocity, we identified the area of the section occupied by reversed (westward) flow stronger than 10 cms^{-1}. For salinity, we computed the average value within the bottom 50 m for the region extending ± 5 km across the shelfbreak; the near-bottom salinity is appropriate for detecting upwelled water. (Temperature could also be used, but since it is not monotonic with depth it is sometimes more difficult to interpret, although this was not the case in the present study.) For wind forcing we used the alongcoast windstress as described above. An upwelling event was identified when the following three criteria were met: (1) easterly winds at Pt. Barrow; (2) the dominant flow in the section was reversed; and (3) the near-bottom salinity was greater than the monthly mean value. These are the same criteria that were used by Spall et al. (2008) to identify the springtime upwelling events in their study.

Since subsequent mooring deployments at the SBI site contained only a single mooring positioned at the center of the boundary current (the BS3 site), it was desirable to develop a technique for identifying the upwelling events using only data from this mooring. Accordingly, for velocity we used the vertically averaged flow between 10-140 m depth at BS3. As demonstrated in Nikolopoulos et al. (2009), this quantity is an excellent proxy for the full transport of the boundary current. For salinity we used the average value over the bottom 50 m at BS3. A salinity anomaly timeseries was then constructed by subtracting the monthly mean value from the instantaneous value for each of the 12 months. For wind forcing we used the same timeseries as that used above. The upwelling events were identified when (1) the wind was easterly; (2) the integrated flow at BS3 was reversed (or strongly weakened); (3) the salinity anomaly at BS3 was positive (or increased noticeably). This method for identifying the upwelling events produced comparable results to the procedure using

the full vertical sections. Consequently, we employed this single mooring approach in the present study. This is partly to provide consistency with future analyses that will use the BS3 data only.

The timeseries of potential temperature and salinity at site BS3 from October 2002 through January 2003 are shown in Fig 4. In the early part of the record (beginning of October) the very warm and fresh water (potential temperature >2°C, salinity <32) is the last remnant of Alaskan Coastal Water flowing by the site. Starting in mid-October one sees a series of warm/salty, bottom-intensified spikes in the record. These are the signature of Atlantic Water upwelling events. We have denoted the most prominent events by black bars at the bottom of the figure. An event is considered prominent when the water at 125 m depth is warmer than 0°C and saltier than 34.4. There are 11 such strong events between mid-October and early December. This information will be used below in characterizing the associated atmospheric storms.

2.2 Meteorological Fields

To describe the storm activity during the fall and early winter of 2002, we used the 6-hourly meteorological re-analysis fields from the National Centers for Environmental Prediction (NCEP) over a domain encompassing much of the North Pacific and western Arctic oceans (see Fig 5). All the storms during the months of September through December were tracked manually using the SLP fields, and at each time step the position of the storm's center was tabulated, as was its central SLP. The tracking procedure and resulting data set are described in detail by Pickart et al. (2009a). Briefly, each 6-hour map was visually inspected to identify all of the low pressure systems in the domain, and storm tracks were constructed by documenting the centers of the lows in successive maps. While automated routines exist to perform this function, we chose to carry it out by hand, partly because of the significant number of interactions between neighboring storms that occur in

this part of the world. We were thus assured of accurately capturing of all the merging events and splitting events that took place over the time period. Future work will address the fidelity by which an automated procedure can reproduce our results. Once this is established, longer time periods (annual to interannual) can be considered without relying on such an arduous and time consuming procedure.

As noted above, Pickart et al. (2009a) used the same data set employed here. However, their study focused on the cyclogenesis of the storms and the associated impacts on the circulation of the North Pacific. Here we address the class of storms that influence the boundary current in the southern Beaufort Sea, resulting in upwelling. The reader should keep in mind that the sample size considered in this study is small: only the fall and early winter 2002 storm season is analyzed. One should therefore be cautious about generalizing the results presented below. However, Pickart et al. (2009a) demonstrated that the development of the storms and their seasonal evolution in the fall and early-winter of 2002 were indicative of the long-term fall climatological conditions.

2.3 Ice concentration

The satellite sea-ice concentration data used in this study come from the Advanced Microwave Scanning Radiometer–Earth Observing System (AMSR-E). Daily images of ice-concentration were constructed using the 19 GHz and 37 GHz vertical and horizontal polarization channels of the passive microwave data. The accuracy of the fields is estimated to be $\pm 10\%$ (Cavelieri et al., 1991), and the native resolution of the AMSR-E sensor is 12.5 km. The data were subsequently interpolated onto a 6.25 km grid. A timeseries of ice-concentration in the vicinity of the mooring array was then constructed for the time period October 2002 through January 2003. This is the average concentration within a 35 km (zonal) by 55 km (meridional) box surrounding the array.

2.4 Ice velocity

Two different ice velocity data sets were used in the analysis. The first is an Arctic-wide product derived from satellite and buoy measurements, and the second is a point timeseries constructed from the upward-facing ADCP on the shoreward-most mooring of the array. The temporal and spatial scales of the two data sets differ significantly, and it is of interest to consider both sources.

2.4.1 Large-scale data

The pan-Arctic sea-ice velocity data set was obtained from the National Snow and Ice Data Center. These are daily ice motion vectors computed using a combination of satellite and in-situ data (predominantly the former). The satellite imagery data come from three sources: the Advanced Very High Resolution Radiometer (AVHRR); the Scanning Multichannel Microwave Radiometer (SMMR); and the Special Sensor Microwave/Imager (SSM/I). The in-situ data are from the International Arctic Buoy Programme (IABP). As described in Fowler (2003), the imagery data are used to compute ice motion following a maximum cross-correlation algorithm (Emery et al., 1995). Optimal interpolation (Isaaks and Srivastava, 1989) is then used to grid the velocities onto a 25 km Equal-Area Scalable Earth Grid (EASE-Grid). Error estimates for the satellite-derived portion of the data were obtained by comparing the vectors to the independent IABP data. The RMS difference between the velocities are on the order of 3-4 cms^{-1}.

We interpolated the ice velocity data from the EASE-Grid onto a spherical coordinate system, with a resolution of 0.25°in latitude and 0.5°in longitude. The ice velocity was then averaged within the same box surrounding the mooring array as was used for the ice concentration, and a timeseries of ice velocity in the alongstream direction was computed.

2.4.2 In-situ data

ADCPs have been shown to be an effective instrument for measuring sea ice motion from a subsurface mooring (e.g. Belliveau, et al., 1989; Melling, et al., 1995). However, due to battery constraints over the year-long deployment, we were unable to invoke the bottom-track mode on the ADCPs, making it more difficult to determine information about the movement of the ice. Nonetheless, we were able to use the water track ping data on the shoreward-most mooring (site BS2, instrument depth of 70 m) to produce a timeseries of ice velocity that appears to be physically plausible and accurate.

The first step was to identify the surface bin, which can often be done by simply using echo intensity. However, the frequent stirring of the bottom sediments during the upwelling events (enhancing the number of scatterers in the lower part of the water column) made this problematic. We instead used the target strength, which scales the echo intensity by an attenuation coefficient. This takes into consideration sound absorption and beam spreading, which are both known quantities for a given ADCP frequency. For the 300 kHz ADCP at mooring BS2, this is 0.062 dBm^{-1} (RD Instruments, 1989). A similar method using target strength to detect the sea floor from echo intensity using water track pings has been used in lowered ADCP data processing (Visbeck, 2002).

Next, the velocity at the maximum target depth was determined. In periods of open water this quantity is noisy and ill-defined, mainly due to the presence of waves and air bubbles near the sea surface. However, in near 100% ice coverage, depending on the nature of the under-ice topography, it is possible to maintain homogeneity of the Doppler shift across all four beams. Therefore, during times of complete ice cover the error velocities were low, indicating that the ADCP-derived ice velocity measurement was accurate. During times of mixed ice coverage the homogeneity argument

may not hold, and in general we found that under these conditions the error velocities were larger and often characterized by spikes. As detailed in Section 3.3, when the ice concentration reached about 50% (according to the satellite ice concentration timeseries at the array site), the ADCP-derived ice velocity appeared to be a meaningful measurement.

3 Results

3.1 Characteristics of Upwelling Storms

A total of 42 individual storms were identified during the four month period of September–December, 2002, and their tracks are shown in Fig 5 (thin cyan lines). Most of the storms entered the domain in the vicinity of Kamchatka (165°E) and initially progressed eastward before spreading out over a much broader range of latitudes. (Five of the storms were Arctic-born cyclones, which are not considered in this study.) For a summary of the general patterns of storm development and spin-down using this data set, the reader is referred to Pickart et al. (2009a). The location of the Beaufort slope moored array is indicated by the black square in Fig 5, and, as seen from the temperature/salinity records of Fig 4, there were numerous upwelling events observed at the site from mid-October to early-December. As noted above, there were 11 major upwelling events during this time frame which are denoted by the black bars in Fig 4. We confine the storm analysis to these significant events.

Aagaard and Roach (1990) presented evidence of eastward phase propagation of upwelling signals along the Beaufort slope using two moorings—one located approximately 50 km upstream (towards Pt. Barrow) of our mooring array, and the other roughly 200 km downstream. This suggests that disturbances originating far to the west might result in upwelling at our array site,

implying that there may not be good correspondence with the local wind field. This was not the case, however, in the 2002-3 data. By far, the majority of the upwelling events detected by the mooring array were associated with easterly wind events recorded by the Pt. Barrow meteorological station. To verify this statistically, we computed the correlation between the alongcoast windstress at Pt. Barrow and the vertically averaged velocity and salinity anomaly timeseries at mooring BS3. Both the velocity and salinity anomaly records were significantly correlated (at the 99% confidence level) with windstress over the year-long deployment. The velocity lagged the wind by 8 hours (r=.60), and the salinity anomaly lagged the wind by 18 hrs (r=.41). This indicates that the boundary current consistently reversed in response to easterly wind events, followed by upwelling of subsurface waters. This relationship is explored further in Section 3.3, including the impact of sea-ice.

The above statistical relationship means that we can use the BS3 temperature/salinity records to identify the individual storms that caused the upwelling events. In particular, the time period of each storm that caused a major upwelling event is given by the corresponding black bar in Fig 4, minus 18 hrs. Using the storm track data we then identified the location of the low pressure system that was responsible for the enhanced easterly winds at the array site. (At times there was more than one Aleutian low present in the domain, but it was always obvious which cyclone was the one in question.) Fig 5 shows the locations of the storms (highlighted in red) that induced significant upwelling at the array site (i.e. the 11 major events in Fig 4). While there is some scatter, a clear trend emerged in that many of the red segments are clustered near the Alaskan Peninsula / eastern Aleutian Island Arc. Consequently we defined a "trigger box" (the large blue square in Fig 5), inside of which storms tended to trigger upwelling in the southern Beaufort Sea.

What are the characteristics of the storms that caused upwelling? To investigate this we constructed composite averages of the SLP and 10 m windspeed for the times that the center of the upwelling storms were within the trigger box of Fig 5 (i.e., for the red segments within the blue box). The SLP composite is shown in Fig 6a, revealing a deep Aleutian low cyclone with a broad spatial extent. This can be thought of as a canonical upwelling storm. The mooring array is marked by the white box in the figure, and, even though the array is located more than 2000 km from the storm center, the isobars are still tightly spaced in that region. Fig 7a shows the corresponding 10 m windspeed composite. There are strong northeasterlies throughout the Chukchi Sea, with a band of enhanced winds extending into the southwestern Beaufort Sea, where they become more easterly (upwelling favorable). Note the channeling of the winds along the southern coast of Alaska and Canada, and the sudden decrease in windspeed over land in that region. This occurs because of the high topography of the coastal region, which gives rise to barrier winds (e.g. Loescher et al., 2006). The impact of orography on the upwelling in the southern Beaufort Sea is explored below.

Note in Fig 5 that there were numerous storms that passed through the trigger box yet did not result in strong upwelling on the Beaufort slope. Fig 6b shows the composite SLP for the time period that those storms passed through the trigger box. Again, the mean field shows an Aleutian low system, but in this case the storm is weaker and more zonally elongated, with less of a meridional extent. Consequently the SLP gradients at the array site are weaker, and the 10 m windspeed is significantly diminished (Fig 7b). The reader should keep in mind that the NCEP reanalysis product has a fairly coarse spatial resolution (approximately 200 km), so the composites of Fig 7 may underestimate the true windspeed. To assess this we tabulated the measured windspeed at the Pt. Barrow meteorological station for the same storm events that comprise the two composites of Fig 7. In the upwelling case, the mean winds at Pt. Barrow were 7.3 ms^{-1} compared with 6.1 ms^{-1}

from NCEP (5.4 ms^{-1} at the array site). For the storms that did not induce upwelling, the mean winds at Pt. Barrow were 2.0 ms^{-1} compared to 1.9 ms^{-1} from NCEP (1.4ms^{-1} at the array site). In all cases the wind direction was approximately 90°T (easterly). Overall, the NCEP winds seem to be fairly representative of the actual winds in this region (at least for the time period considered). These results imply that, on average, an increase in windspeed from 2 ms^{-1} to 6-7 ms^{-1} results in a significant upwelling event on the continental slope of the Alaskan Beaufort Sea.

Inspection of the trajectories of the individual storms that make up the two composites of Figs 6 and 7 sheds light on why the far-field winds are different in the upwelling versus non-upwelling cases. As seen in Fig 8, the storms that induced upwelling on the Beaufort slope tended to divert to the north: all but two of the storms exited the domain north of 65°N (four of them ultimately entered the Arctic Ocean). By contrast, the non-upwelling storms traveled more zonally through the North Pacific, with only one of them (briefly) passing north of 65°N. The upper level steering flow partially explains this discrepancy in storm tracks. In particular, Fig 9 shows the same two SLP composites (color), overlain by the 500 mb height field (contours). In the upwelling case there is a sharp bend in the 500 mb height contours, implying that the steering currents advected the storms significantly to the north. For the non-upwelling case the flow aloft is more zonally oriented, with only a weak bend in the height contours. This suggests that upwelling in the southern Canada Basin is more apt to occur not only if the Aleutian lows are deep, but if they also progress significantly northward as they travel across the North Pacific.

3.2 Northward Progression of Storms

Although on average the tracks of Aleutian lows extend from west to east in association with the North Pacific sea surface temperature front, there are a variety of distinct patterns that the storms

follow. For example, Anderson and Gyakum (1989) identified a regime in which the storms tend to progress directly into the Bering Sea. This in turn has ramifications for the development of the pack-ice in the Bering Sea (Overland and Pease, 1982). Another well-known pattern is a northward-directed track bringing storms into the Gulf of Alaska from the south (Terada and Hanzawa, 1984; Wilson and Overland, 1986; Pickart et al., 2009a). On interannual timescales, the strength of the Aleutian low varies strongly, as measured by the North Pacific Index (NPI, see Trenberth and Hurrell, 1994). Rodionov et al. (2005) showed that there are significant differences in storm tracks associated with high and low periods of the NPI. In the present context of upwelling along the Beaufort continental slope, we are interested in why certain storms progress north of about 65°N, or roughly the latitude of Bering Strait (see Fig 8a). While the upper-level steering flow composites of Fig 9 are enlightening, there are a number of different factors that dictate how far north a Pacific-born cyclone will go. For example, a blocking pattern set up by the Siberian high can inhibit storms from traveling northward (see Overland and Hiester (1980) and Section 3.3 below). The orography of the land can also strongly influence the fate of the storms (see for example Asuma et al., 1998). In this regard, a more detailed examination of the northward progressing storms in the present data set offers further insight.

A fairly common effect of topography on the movement and development of storms is the process known as lee cyclogenesis. Essentially, as a storm approaches a topographic barrier, the lower part of the system is blocked while the upper portion continues relatively unimpeded, advected by the cross-barrier steering currents aloft. On the lee side of the barrier the surface low can then re-establish itself. This process has been explained by the development of a standing baroclinic lee wave where the first trough downwind of the barrier strengthens in time (Smith, 1984). The subsequent surface low that forms is known to travel significant distances away from the barrier

(Chung et al., 1976). Lee cyclogenesis occurs at numerous locations around the world, for instance in the Alps (Buzzi and Tibaldi, 1978) and the Canadian Rocky Mountains (Chung et al., 1976). It also occurs as a result of the orography of Alaska. Lynch et al. (2001) discuss evidence for, and the conditions surrounding, lee cyclogenesis associated with the Alaska Range near 60-64°N and the Brooks Range near 68°N (see Fig 10). Their analysis focused on the development of storms along two distinct Arctic frontal zones during summer. Evidence for lee cyclogenesis caused by the Brooks Range was also presented for the winter months (see also Lynch, 1997).

Of particular relevance to our study, Asuma et al. (1998) diagnosed a lee cyclogenesis event in September 1994 during the Beaufort and Arctic Storms Experiment (BASE). The event in question consisted of a Pacific-born cyclone (of the type discussed above), impinging on the high topography of the Mackenzie mountains (Fig 10) and subsequently forming a smaller lee cyclone that deepened rapidly and progressed into the southern Beaufort Sea. One of the consequences of such topographic blocking is that low-level moisture, originating from the Pacific and advected northward by the storm, is inhibited from progressing into the Arctic domain. As part of BASE, timeseries data were collected at a station on the Canadian Beaufort coast near 133°W, and Asuma et al. (1998) noted that many of the high wind speed events measured during the study were due to Pacific-origin storms. This is consistent with our results, suggesting that such Aleutian low systems regularly impact the Alaskan Beaufort shelf and slope.

Detailed examination of the northward progressing storms in our data set suggests that lee cyclogenesis may play a role in the ability of the Aleutian lows to expand their northward influence and induce upwelling in the southern Canada Basin. During fall and early-winter 2002, six storms progressed north of 70°N into the Arctic ocean. Five of these storms experienced some degree of lee cyclogenesis—two occurrences associated with the Alaska range, and three associated with the

Brooks range. Fig 10 shows an example of each type. In both cases the flow in the mid-troposphere was directed across the barrier, and the surface low that split off from the parent storm developed in the lee of the mountain range. Four of the five events (all of the ones after September) were associated with upwelling at the array site. Admittedly our sample size is small, and consideration of additional years is required to document how persistent this phenomenon is. Our results suggest, however, that orography may be an important factor in the upwelling process on the Beaufort slope.

3.3 Inhibiting Upwelling

As seen in Fig 4, the upwelling activity at the mooring array site diminished markedly starting in early December, 2002. Both the frequency and the strength of the events decreased. However, there was no obvious change in the Aleutian low storm activity during that time. What then caused this change in upwelling? We discuss two possibilities: modulation of the upwelling signal due to ice cover, and impact on the spatial extent of the storms due to upper-level atmospheric circulation patterns.

3.3.1 Ice Cover

The Alaskan Beaufort shelf and slope are often ice-free in late-summer/early-fall, and in 2002 this was the case. According to the satellite record, freeze-up occurred at the mooring site from late-October to early-December (Fig 11a). The normal progression is for pancake ice to form first, which then transforms and thickens into gray ice, white ice, and finally first year ice which is typically 1-2 m thick. During the early stages of formation the pack-ice tends to be fairly smooth, but, as time progresses, ridging and deformation occur which can cause a quite irregular keel. Unfortunately, in the present study we have no information regarding the thickness of the ice in the region of

the mooring array. In a subsequent field program, however, an upward-looking sonar was used to obtain timeseries of ice draft, and it was found that keels were typically 1-3 m over much of the winter season (there were, however, instances of substantial ridging to depths of 10 m).

Once ice forms (or is transported into the region), the windstress no longer acts directly on the sea surface but instead imparts momentum to the pack-ice. The movement of the ice—which itself is subject to various forces including internal ice stresses—then forces the ocean. The exception to this is in the landfast ice zone, where the ocean is shielded from the direct influence of the wind. In the Beaufort Sea, the landfast ice typically extends to the vicinity of the 20 m isobath (Mahoney et al., 2007), well inshore of our array site. However, on occasion it is found much farther offshore. Using 9 years of Synthetic Aperture Radar data, Mahoney et al. (2007) produced timeseries of the seaward landfast ice extent (SLIE) along the Alaskan Beaufort Sea. During stable extension events it was found that the fast ice could extend significantly beyond the shelfbreak. Using the SLIE product, A. Mahoney (pers. comm., 2009) constructed a timeseries for the region near the mooring array for winter 2002-3. For the time period considered here (September 2002–January 2003) the landfast ice was confined to bottom depths less than 20 m, hence it was not a factor in the modulation of the upwelling signal observed by the array.

There are various complicating factors that make it challenging to quantify the influence of the pack-ice on the Beaufort shelfbreak current during the wind events in question. These include the thickness of the ice pack and the roughness of its top and bottom edges, which impact the drag on the water. Furthermore, in the marginal ice zone and in temporary leads and polynyas, the wind acts both on the ice and the neighboring open water. Despite these complications, a clear story seemed to emerge regarding the role of the ice in the upwelling response at the array site during our period of study. Fig 11b shows the ice velocity measured by the ADCP in comparison

to the error velocity. One sees that the error velocity, although somewhat larger in the beginning of the record during freeze-up, is small compared to the velocity of the ice (note the difference in the y-axis scales of Fig 11b). Of note are the large ice speeds measured during much of November, including one period where the velocity exceeded 1.5 ms^{-1}. Once freeze-up is complete, around the beginning of December, the periods of enhanced ice velocity in the record correspond to detectable dips in the ice concentration (e.g. notice the two episodes in January 2003).

The satellite-derived ice velocity is compared with the ADCP-derived value in Fig 11c. While the two timeseries are clearly correlated, there is a discrepancy in the amplitude of the signals. This is partly because of the difference in the scales of the two measurements. The spatial resolution of the satellite is 25 km, which is on the order of the width of the shelfbreak current, and there is inherent smoothing during the satellite processing. In contrast, the ADCP provides a point measurement. This probably explains the difference between the two records from mid-December through January when the ice concentration is near 100%. However, during the period of freeze-up, it is likely that the satellite record severely underestimates the true ice motion. In general, satellite-derived ice velocities are suspect in regions of new ice growth and in the marginal ice zone, because the procedures are less robust with less ice present. Also, calibration/verification studies using ice buoy data are not possible under these conditions (C. Fowler, pers. comm., 2009). In the present case, the measured velocity of the water at the shallowest good ADCP bin underneath the ice (10-15 m depth) far exceeds the satellite-derived ice velocity during the period of freeze-up, while at the same time it is consistently less than the ADCP-derived ice velocity. For these reasons, we take the ADCP-derived timeseries to be a more accurate measure of the true ice motion.

During the period of freeze-up from late October to the beginning of December the upwelling events were frequent and strong (Fig 4). As noted above, however, shortly after the ice cover

approached 100% (and stayed near that level) the strength of the upwelling events decreased, as did their frequency. It is likely that the amplitude change was due to the presence of the pack-ice, but we argue that the change in frequency was not. Fig 12a shows the ADCP-derived ice velocity in relation to the windstress at Pt. Barrow. It is readily apparent from the relationship between the two timeseries that the pack-ice responded to all of the easterly wind events during the entire record, irregardless of the ice concentration. That is, there was not a single instance when a storm did not set the ice in motion which in turn would transmit stress to the water column. This provides compelling evidence that the presence of pack-ice did not cause the decrease in the number of recorded upwelling events at the mooring array after the first of December.

Did the pack-ice modulate the amplitude of the upwelling response? To assess this we considered the timeseries of vertically averaged alongstream velocity and salinity anomaly at the center of the boundary current (mooring BS3, Fig 12b). As discussed above, these quantities are appropriate measures of the strength of the reversed flow of the shelfbreak current and magnitude of the subsequently upwelled water due to the storms. To obtain a single measure of the ocean response, we calculated the empirical orthogonal functions (EOFs) for the two timeseries. In light of the statistical relationship noted above between the two variables, the velocity timeseries was first adjusted forward by 8 hours and the salinity anomaly timeseries by 18 hours to match the signals with each other and with the windstress timeseries (the windstress was not used in the EOF, since it represents the forcing).

The dominant EOF mode accounts for 70% of the variance and can be interpreted as an "upwelling amplitude" timeseries (Fig 13). An upwelling event was defined when an easterly wind is followed by a reversal of the boundary current to the west (or a pronounced weakening of the eastward flow) and a significant increase of the near-bottom salinity. In addition, the absolute

value of the EOF amplitude had to be greater than 0.1 and the windstress had to exceed .04 Nm^{-2}. These criteria produced comparable results to the detection methods described above (Section 3.1), except that we now have a single explicit measure of the strength of the water column response. Each of the upwelling events over the period of the study is marked by a square symbol in Fig 13. Keep in mind that the two timeseries in Fig 13 are independent—one represents the forcing, and the other represents the response.

Inspection of Fig 13 indicates that there is a weakening in the upwelling strength after freeze-up is complete and the ice cover is near 100% (after the first of December). This is true even though there is no systematic decrease in the strength of the wind forcing. To quantify this we computed regressions between the windspeed and EOF amplitude (the events marked by the squares in Fig 13) before and after the onset of complete ice cover in early December. During the period of freeze-up, an easterly wind speed of 10 ms^{-1} results in a flow reversal of 32 cms^{-1} to the west. Keep in mind that this is the vertically integrated flow over the water column. Using the transport proxy defined by Nikolopoulos et al. (2009), this equates to a transport of .9 Sv to the west. Correspondingly, there is an increase in near-bottom salinity of .98. In contrast, after the ice cover is fully established, an easterly wind speed of 10 ms^{-1} causes a flow reversal of only 16 cms^{-1} (.45 Sv) and an increase in salinity of .41.

3.3.2 Atmospheric blocking

The results of the previous section imply that, while the presence of near 100% pack-ice dampens the response of the oceanic upwelling in the Beaufort shelfbreak current, it does not diminish the frequency of these events (provided the landfast ice does not extend out to the shelfbreak). Hence, to explain the dearth of upwelling observed by the mooring array during the months of December

and January, we must look elsewhere. (Recall that the Aleutian low storm activity in the North Pacific did not decrease during this time.) Inspection of the NCEP fields suggests that there were likely two factors involved, both related to the upper-level atmospheric steering flow. As mentioned above (Section 3.2), a well known atmospheric blocking pattern during winter is often established by the Siberian high and a ridge that extends southeastward from it (see for example Overland and Hiester, 1980, and figure 2-1 of Wilson and Overland, 1986). When this happens, storms are inhibited from progressing northward towards the Arctic domain. During December 2002 such a pattern established itself. As a result, three storms passed through the trigger box of Fig 5 that should have been deep enough to cause strong upwelling but did not. The composite SLP and 500 mb height field of these three storms are shown in Fig 14a. Note that the central surface pressure of the composite Aleutian low is as deep as the canonical upwelling storm of Fig 5a. However, the strong signature of the Siberian high—extending well into the troposphere—caused an effective block, and consequently the winds were weak at the mooring site.

In January 2003 the Siberian high weakened and the upper-level air patterns changed, but the northward influence of the Aleutian lows was still inhibited. A second well-known wintertime blocking pattern in the North Pacific consists of a stationary surface high and associated ridge aloft that is often found in the central part of the basin (White and Clark, 1975; Wilson and Overland, 1986). Using data over a 14-yr period, Dole and Gordon (1983) established a climatology of persistent wintertime features in the 500 mb height field over the northern hemisphere. In general, negative anomalies were due to transient storms, while positive anomalies were associated with quasi-stationary ridges. In the North Pacific, a blocking pattern was frequently found in the central basin, south of the Alaskan peninsula. This is not surprising since blocks tend to occur in regions where cyclone activity is high (Pelly and Hoskins, 2003). Dole and Gordon's (1983) climatology is

consistent with the earlier study of White and Clark (1975) who investigated wintertime blocking activity in the North Pacific for the period 1950–70. White and Clark (1975) found that the blocking events were most common in the month of January. One of the consequences of this is that Aleutian lows would tend to be diverted to the north or south as they progress across the north Pacific basin (Wilson and Overland, 1986).

It is natural then to ask if the continued reduction of upwelling in January 2003 was due to blocking activity in the central basin. Fig 14b shows the composite SLP and 500 mb height field for the five strong January storms that passed through the trigger box of Fig 5, yet did not cause upwelling. (As was true in December, these storms were as deep as the canonical upwelling storm of Fig 5a.) One sees that the high surface pressure north of Siberia is reduced from the December composite, but now there is a pronounced ridge at 500 mb extending from northwest Canada all the way to the Siberian continent. This ridge is clearly inhibiting the northward influence of the Aleutian lows, resulting in light winds at the mooring site. We suspect, however, that the feature in question is not a North Pacific blocking ridge of the type discussed above. While that class of ridge can occasionally be found on the eastern side of the basin (e.g. Dole and Gordon, 1983; Wilson and Overland, 1986), it is typically located in the central North Pacific. By contrast, the ridge in Fig 14b is situated far to the east, and the surface high is located over the Canadian continent. It is more likely that the ridge seen here is a manifestation of the climatological North American ridge (e.g. Rodionov et al., 2005). This quasi-permanent feature arises because of the difference in heating between the ocean and land, as well as the orography of western North America and Canada (Rodionov et al., 2005; see also Held et al., 2002). On interannual timescales the North American ridge strengthens and weakens due to various factors, including sea surface temperature, pack-ice, and internal atmospheric dynamics (Rodionov et al., 2005). While it is beyond the scope

of our study to identify the precise cause, it appears that the North American ridge was especially pronounced during the month of January 2003, limiting the ability of the Aleutian lows to induce upwelling in the southern Beaufort Sea.

4 Summary and Discussion

Using meteorological re-analysis fields and water column and ice data collected from a mooring array in fall/winter 2002, the atmospheric conditions leading to upwelling in the Alaskan Beaufort Sea were elucidated, as was the oceanographic response. It appears that there is a preferred set of circumstances in which Aleutian low pressure systems induce upwelling along the continental slope. This happens when the cyclones are located in the vicinity of the eastern Aleutian Island Arc and Alaskan Peninsula. The canonical upwelling storm is deep, has a wide meridional extent, and its trajectory tends to the north. This northward progression is consistent with the upper-level steering flow, although the formation of a secondary low from lee cyclogenesis associated with the orography of Alaska can also expand the northward influence of the storms.

Starting in early December, and lasting through January, both the intensity and frequency of the upwelling diminished even though the Aleutian low storm activity in the North Pacific remained high. It was argued that the reduced upwelling amplitude was due to the onset of heavy pack-ice (near 100% concentration), but this can't explain the decrease in number of events. The landfast ice edge was located far inshore of the array during this time period, and the ice velocity timeseries from the mooring array revealed that the mobile pack-ice was able to transmit stress to the water column during each of the storms. It is worth noting, however, that later in the winter the landfast ice did extend to the array site for roughly a five-week period (A. Mahoney, pers. comm.

2009). Future analysis is necessary to see how this in turn impacted the upwelling. The change in upwelling frequency after the first of December is explainable by a combination of different upper-level atmospheric blocking patterns that limited the northward influence of the storms. The first blocking pattern, present throughout December, consisted of a pronounced Siberian high and a ridge of high pressure extending to the southeast. The second pattern, dominant in January, was characterized by an enhanced North American ridge that isolated the mooring site from the influence of the Aleutian lows.

While the composites of Fig 9 reveal the synoptic conditions associated with upwelling and no upwelling respectively, it is interesting to note that these two configurations are similar to the two interannual states of the North Pacific storm climate described by Rodionov et al. (2005). In particular, the upwelling case of Fig 9a is strongly reminiscent of the low NPI state of Rodionov et al.(2005). This includes a deeper Aleutian surface low, a pronounced northward bend in the upper level steering flow, and more northward directed storm tracks. Conversely, the non-upwelling case of Fig 9b is similar to the high NPI state, with a weaker Aleutian surface low, more zonally oriented steering currents, and storm tracks progressing eastward in the eastern part of the basin. This suggests that there may be prolonged periods, lasting years or longer, that may be characterized by enhanced or diminished upwelling in the southern Beaufort Sea (as reflected in the North Pacific Index). Our results imply, however, that there is a potentially complicating factor involving the North American ridge. As Rodionov et al. (2005) point out, the enhancement of the North American ridge in the low NPI state (strong Aleutian low) helps direct the storms northward, which is indeed conducive for upwelling (Fig 9a). However, if the ridge becomes too pronounced it may act as a block, as was the case in January 2003 (Fig 14b). This in turn would inhibit the upwelling, even in a low NPI state. Hence, at present it is not obvious how a varying Pacific storm

climate, e.g. due to global warming, will impact upwelling in the Alaskan Beaufort Sea. We will soon obtain a fourth year of mooring data from the same location on the Beaufort slope, which will allow us to address a wider range of timescales and environmental conditions, and hence further our understanding of the atmosphere-ocean-ice system in this regard.

Acknowledgments

The authors thank Elizabeth Hunke and Miles McPhee for helpful discussions on ice-ocean interaction, Humfrey Melling for insights about measuring ice velocity, Chuck Fowler for informative discussions about the satellite ice motion data set, Seth Danielson for processing the meteorological data from the Pt. Barrow weather station, Tom Agnew for providing the ice concentration data, and Andy Mahoney for performing the landfast ice calculation. The following grants provided support for this study. National Science Foundation grants OPP-0731928 (RP) and OPP-0713250 (RP and PF); Office of Naval Research grant N00014-07-1-1040 (DT and RG); Natural Sciences and Engineering Research Council of Canada (GWKM); Woods Hole Oceanographic Institution Arctic Initiative (JY). Any opinions, findings, and conclusions or recommendations expressed in this material are those of the authors and do not necessarily reflect the views of the the National Science Foundation.

References

Aagaard, K., L.K. Coachman and E.C. Carmack, 1981. On the halocline of the Arctic Ocean. *Deep-Sea Research*, **28**, 529–545.

Aagaard, K. and A.T. Roach, 1990. Arctic ocean-shelf exchange: measurements in Barrow Canyon. *Journal of Geophysical Research*, **95**, 18,163–18,175.

Anderson, J.R. and J.R. Gyakum, 1989: A diagnostic study of Pacific basin circulation regimes as determined from extratropical cyclone tracks. *Monthly Weather Review*, **117**, 2672–2686.

Belliveau, D.J., G.L. Bugden, and S.G.K. Melrose, 1989: Measurement of sea ice motion using bottom mounted Acoustic Doppler Current Profilers, *Sea Technology*, **30**, 10-12.

Asuma, Y., S. Iwata, K. Kikuchi, G.W.K. Moore, R. Kimura, and K. Tsuboki, 1998: Precipitation features observed by Doppler radar at Tuktoyaktuk, Northwest Territories, Canada, during the Beaufort and Arctic storms experiment. *Monthly Weather Review*, **126**, 2384–2405.

Bourke, R.H. and R.G. Paquette, 1976: Atlantic water on the Chukchi shelf. *Geophysical Research Letters*, **3**, 629–632.

Buzzi, A. and S. Tibaldi, 1978: Cyclogenesis in the lee of the Alps: A case study. *The Quarterly Journal of the Royal Meteorological Society*, **104**, 271–287.

Carmack, E.C. and E.A. Kulikov, 1998: Wind-forced upwelling and internal Kelvin wave generation in Mackenzie Canyon, Beaufort Sea. *Journal of Geophysical Research*, **103**, 18,447–18,458.

Cavalieri, D.J, J.P. Crawford, M.R. Drinkwater, D.T. Eppler, L.D. Farmer, R.R. Jentz, and C.C. Wackerman, 1991: Aircraft active and passive microwave validation of sea ice concentration from the DMSP SSM/I. *Journal of Geophysical Research*, **96**, 21,989–22,008.

Chung, Y-S., K.D. Hage, and E.R. Reinelt, 1976: On lee cyclogenesis and airflow in the Canadian Rocky Mountains and the East Asian Mountains. *Monthly Weather Review*, **104**, 879–891.

Dole, R.M. and N.D. Gordon, 1983: Persistent anomalies of the extratropical northern hemisphere wintertime circulation: Geographical distribution and regional persistence characteristics. *Monthly Weather Review*, **111**, 1567–1586.

Emery, W., C. Fowler, and J. Maslanik. 1995: Satellite remote sensing of ice motion, in Oceanographic Applications of Remote Sensing, ed. Motoyoshi Ikeda and Frederic W. Dobson. CRC Press, Boca Raton.

Favorite, F., A.J. Dodimead, and K. Nasu, 1976: Oceanography of the subarctic Pacific region, 1962-72. *Bull. Int. North Pac. fish. comm.*, **33**, 1-187.

Fowler, C. 2003: Polar Pathfinder Daily 25 km EASE-Grid Sea Ice Motion Vectors. Boulder, Colorado USA: National Snow and Ice Data Center. Digital media. (ftp://sidads.colorado.edu/pub/DATASETS/
icemotion), updated in 2007.

Grebmeier, J.M., and H.R. Harvey, 2005: The Western Arctic Shelf-Basin Interactions (SBI) Project: An Overview. *Deep-Sea Research II*, **52**, 3109–3115.

Gyakum, J.R., J.R. Anderson, R.H. Grumm, and E.L. Gruner, 1989: North Pacific cold-season surface cyclone activity: 1975-1983. *Monthly Weather Review*, **117**, 1141–1155.

Held, I.M., M. Ting, and H. Wang, 2002: Northern winter stationary waves: Theory and modeling. *Journal of Climate*, **15**, 2125–2144.

Isaaks, E., and R.M. Srivastava. 1989: An introduction to applied geostatistics. New York: Oxford University Press.

Ivanov, V.V., G.I. Shapiro, J.M. Huthnance, D.L. Aleynik, and P.N. Golovin, 2004: Cascades of dense water around the world ocean. *Progress in Oceanography*, **60**, 47–98.

Kämpf, J., 2005: Cascading-driven upwelling in submarine canyons at high latitudes. *Journal of Geophysical Research*, **110**, doi:10.1029/2004JC002554.

Llinas, L., R.S. Pickart, J.T. Mathis, and S.L. Smith, 2009: Zooplankton inside an Arctic Ocean cold-core eddy: Probable origin and fate. *Deep-Sea Research II*, doi:10.1016/j.dsr2.2008.10.020.

Large, W. G., and S. Pond, 1981: Open ocean momentum flux measurements in moderate to strong winds. *Journal of Physical Oceanography*, **11**, 324336.

Loescher, K. A., G. S. Young, B. A. Colle, and N. S. Winstead, 2006: Climatology of Barrier Jets along the Alaskan Coast. Part I: Spatial and Temporal Distributions. *Monthly Weather Review*, **134**, 437–453.

Lynch, A.H., 1997: Topographically generated gravity waves in the Brooks Range, Alaska. *Geophysical Research Letters*, **24**, 2981–2984.

Lynch, A.H., A.G. Slater, and M. Serreze, 2001: The Alaskan Arctic frontal zone: Forcing by orography, coastal contrast, and the boreal forest. *Journal of Climate*, **14**, 4351–4362.

Mahoney, A., H. Eicken, A.G. Gaylord, and L. Shapiro, 2007: Alaska landfast sea ice: Links with bathymetry and atmospheric circulation. *Journal of Geophysical Research*, **112**, doi:10.1029/2006JC003559.

Mathis, J.T., R.S. Pickart, D.A. Hansell, D. Kadko, and N.R. Bates, 2007: Eddy transport of organic carbon and nutrients from the Chukchi shelf into the deep Arctic basin. *Journal of Geophysical Research*, **112**, 10.1029/2006JC003899.

Melling, H., P. H. Johnston, and D. A. Reidel, 1995: Measurement of the underside topography of sea ice by moored subsea sonar. *Journal of Atmospheric and Oceanic Technology*, **12**, 589-602.

Mountain, D.G., L.K. Coachman, and K. Aagaard, 1976: On the flow through Barrow Canyon. *Journal of Physical Oceanography*, **6**, 461–470.

Nikolopoulos, A., R. S. Pickart, P. S. Fratantoni, K. Shimada, D. J. Torres, and E. P. Jones, 2009: The western Arctic boundary current at 152°W: Structure, variability, and transport. *Deep-Sea Research II*, doi:10.1016/j.dsr2.2008.10.014.

Overland, J.E. and C.H. Pease, 1982: Cyclone climatology of the Bering Sea and its relation to sea ice extent. *Monthly Weather Review*, **110**, 5-13.

Overland, J.E. and R.T. Hiester, 1980: Development of a synoptic climatology for the Northeast Gulf of Alaska. *Journal of Applied Meteorology*, **19**, 1-14.

Paquette, R. G. and R. H. Bourke, 1974. Observations on the coastal current of Arctic Alaska. *Journal of Marine Research*, **32**, 195–207.

Pelly, J.L. and B.J. Hoskins, 2003: A new perspective on blocking. *Journal of the Atmospheric Sciences*, **60**, 743–755.

Pickart, R.S., 2004: Shelfbreak circulation in the Alaskan Beaufort Sea: Mean structure and variability. *Journal of Geophysical Research*, **109**, doi:10.1029/2003JC001912.

Pickart, R.S., T.J. Weingartner, L.J. Pratt, S. Zimmermann, D.J. Torres, 2005: Flow of winter-transformed water into the western Arctic. *Deep Sea Research II*, **52**, 3175-3198.

Pickart, R. S., G. W. K. Moore, A. M. Macdonald, I. A. Renfrew, J. E. Walsh, and W. S. Kessler, 2009a: Seasonal evolution of Aleutian low-pressure systems: Implications for the North Pacific sub-polar circulation. *Journal of Physical Oceanography*, in press.

Pickart, R. S., L. J. Pratt, D. J. Torres, T. E. Whitledge, A. Y. Proshutinsky, K. Aagaard, T. A. Agnew, G. W. K. Moore, H. J. Dail, 2009b: Evolution and dynamics of the flow through Herald Canyon in the Western Chukchi Sea. *Deep Sea Research II*, in press.

RD Instruments, 1989: Acoustic Doppler Current Profilers Principles of Operation: A Practical Primer. RD Instruments, 51 pp.

Rodionov, S.N., J.E. Overland, and N.A. Bond, 2005: Spatial and temporal variability of the Aleutian climate. *Fisheries Oceanography*, **14**, 3–21.

Signorini, S.R., A. Munchow, and D. Haidvogel, 1997: Flow dynamics of a wide Arctic canyon. *Journal of Geophysical Research*, **102**, 18,661–18,680.

Smith, R.B., 1984: A theory of lee cyclogenesis. *Journal of Atmospheric Sciences*, **41**, 1159–1168.

Spall, M.A., R. S. Pickart, P. Fratantoni, and A. Plueddemann, 2008: Western Arctic Shelfbreak Eddies: Formation and transport. *Journal of Physical Oceanography*, **38**, 1644-1668.

Terada, K. and M. Hanzawa, 1984: Climate of the North Pacific Ocean, in Climates of the oceans, edited by H. Van Loon, pp. 431-477. World Survey of Climatology, Vol 15. Elsevier, New York.

Trenberth, K.E. and J.w. Hurrell, 1994: Decadal atmosphere-ocean variations in the Pacific. *Climate Dynamics*, **9**, 303-19.

Visbeck, M., 2002: Deep velocity profiling using Lowered Acoustic Doppler Current Profilers: Bottom track and inverse solutions. *Journal of Atmospheric and Oceanic Technology*, **19**, 794807.

Weingartner, T.J., D.J. Cavalieri, K. Aagaard, and Y. Sasaki, 1998: Circulation, dense water formation, and outflow on the northeast Chukchi shelf. *Journal of Geophysical Research*, **103**, 7647–7661.

White, W.B. and N.E. Clark, 1975: On the development of blocking ridge activity over the central North Pacific. *Journal of the Atmospheric Sciences*, **32**, 489–502.

Wilson, J.G. and J.E. Overland, 1986. Meteorology. In: Hood, D.W., Zimmerman, S.T. (Eds.), The Gulf of Alaska, Physical Environment and Biological Resources. Alaska Office, Ocean Assessments Division, National Oceanic and Atmospheric Administration, US Department of Commerce, 655pp.

Woodgate, R.A., K. Aagaard, T.J. Weingartner, 2005: A year in the physical oceanography of the Chukchi Sea: Moored measurements from autumn 1990–1991. *Deep-Sea Research II*, **52**, 3116-3149.

Yang, J., 2006: The seasonal variability of the Arctic ocean Ekman transport and its role in the mixed layer heat and salt fluxes. *Journal of Climate*, **19**, 5366–5387.

Zhang, X., J.E. Walsh, J. Zhang, U.S. Bhatt, and M. Ikeda, 2004: Climatology and interannual variability of Arctic cyclone activity: 1948-2002. *Journal of Climate*, **17**, 2300–2317.

Figure Captions

Figure 1 Schematic circulation of the Chukchi and Beaufort Seas (after Spall et al, 2008). Included is the location of the mooring array that measured the shelf-edge current north of Alaska. On average the boundary current flows to the east, but under easterly, upwelling winds the flow reverses to the west.

Figure 2 The SBI Beaufort slope mooring array (from Spall et al., 2008). Mooring names are indicated along the top, and the instrumentation used is listed in the key.

Figure 3 Vertical sections from the mooring array. The left-hand panels are velocity (cms^{-1}), and the right-hand panels are potential temperature (color, °c) with salinity (contours) overlaid. Positive velocity is along 125°T. The top row contains the year-long mean sections over the time period 2 August 2002 – 31 July 2003 (from Nikolopoulos et al., 2009), and the bottom row is a snapshot from an upwelling event in early November, 2002.

Figure 4 Timeseries of (a) potential temperature and (b) salinity at mooring BS3 in the center of the boundary current. The warm/salty bottom-intensified spikes are due to upwelling events (see Fig 3, bottom panel). The time periods corresponding to the 11 major events are indicated by the thick black lines along the bottom of the plot.

Figure 5 Storm tracks (cyan lines) during fall 2002. The blue circles indicate the first point, and the magenta circles denote the last point. The red segments indicate the locations of the parent cyclones when upwelling occurred at the mooring site (black square). The blue square is the trigger box used to construct the composite fields (see text).

Figure 6 Composite sea level pressure fields (mb). The location of the mooring array is indicated by the white square. (a) Composite corresponding to the red segments (upwelling) of the

cyclones within the trigger box of Fig 5. (b) Composite corresponding to cyan portion (no upwelling) of the storms within the trigger box.

Figure 7 Composite 10 m windspeed fields (ms^{-1}, color), with the wind vectors overlaid. The location of the mooring array is indicated by the white square. (a) Composite corresponding to the red segments (upwelling) of the cyclones within the trigger box of Fig 5. (b) Composite corresponding to cyan portion (no upwelling) of the storms within the trigger box.

Figure 8 (a) Tracks of storms that passed through the trigger box (Fig 5) and caused upwelling at the array site. Symbols are the same as in Fig 5. (b) Tracks of storms that passed through the trigger box and did not result in upwelling.

Figure 9 The same composite sea level pressure fields (color, mb) as in Fig 6, except that the composite 500 mb height fields (contours in meters) are overlaid. The first and last points of the storms comprising the composites are indicated by the circles (as in Fig 5).

Figure 10 Two instances of lee cyclogenesis during fall 2002. The contours show the composite 500 mb height field just prior to when the lee cyclone formed. The black star denotes the location of the parent cyclone at the end of the composite, and the red star shows where the lee cyclone formed over the next 6-hr period. The topography of the land (in meters) is colored. (a) Alaska Range lee cyclogenesis. The composite period is 20 Oct 12Z – 21 Oct 0Z. (b) Brooks Range lee cyclogenesis. The composite period is 26 Oct 12Z – 27 Oct 0Z.

Figure 11 (a) Timeseries of average ice concentration within a 35 km (zonal) by 55 km (meridional) box surrounding the array. (b) Component of ice velocity in the alongstream direction (negative is westward) from the ADCP (blue) and error velocity (cyan) at mooring BS2. (c) ADCP ice velocity from (b) compared with the satellite-derived ice velocity in the alongstream

direction (red), which is the average value within the same box used for the ice concentration in (a).

Figure 12 (a) ADCP-derived alongstream ice velocity from Fig 11b (blue) compared with the alongcoast windstress from the Pt. Barrow meteorological station (green). (b) Vertically averaged (10-140 m) alongstream velocity at mooring BS3 (black) compared with the vertically averaged (over the bottom 50 m) salinity anomaly (magenta). The velocity timeseries has been moved forward by 8 hours and the salinity anomaly by 18 hours to align them with the windstress (see text).

Figure 13 (a) Alongcoast windstress from Fig 12a, where the upwelling events are indicated by the square symbols. (b) Timeseries of EOF mode 1, which is defined as the Upwelling Amplitude. The upwelling events are marked by the squares. (Note that the time of each event corresponds to the peak in forcing, which can vary slightly from the peak in response, since they are independent timeseries.)

Figure 14 Composite sea level pressure (color, mb) overlaid by 500 mb height (contours in meters) of the (a) three storms in December 2002 and (b) five storms in January 2003 that did not result in upwelling at the array site (white square) while within the trigger box of Fig 5.

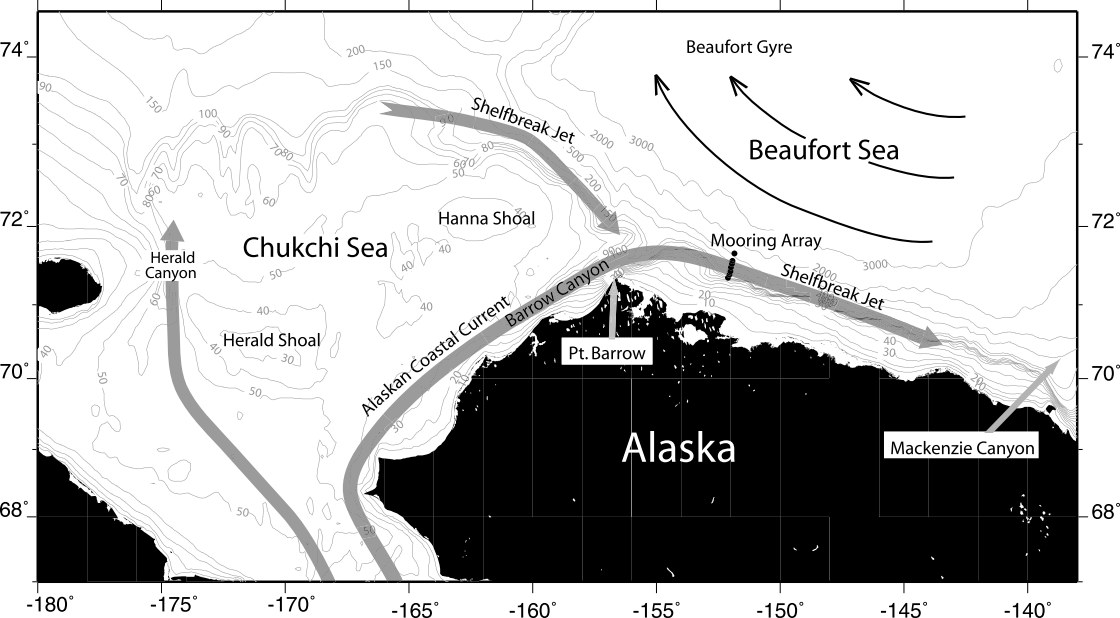
Beaufort Gyre
Beaufort Sea
Shelfbreak Jet
Chukchi Sea
Hanna Shoal
Herald Canyon
Herald Shoal
Mooring Array
Shelfbreak Jet
Barrow Canyon
Alaskan Coastal Current
Pt. Barrow
Alaska
Mackenzie Canyon
74˚
72˚
70˚
68˚
-180˚
-175˚
-170˚
-165˚
-160˚
-155˚
-150˚
-145˚
-140˚

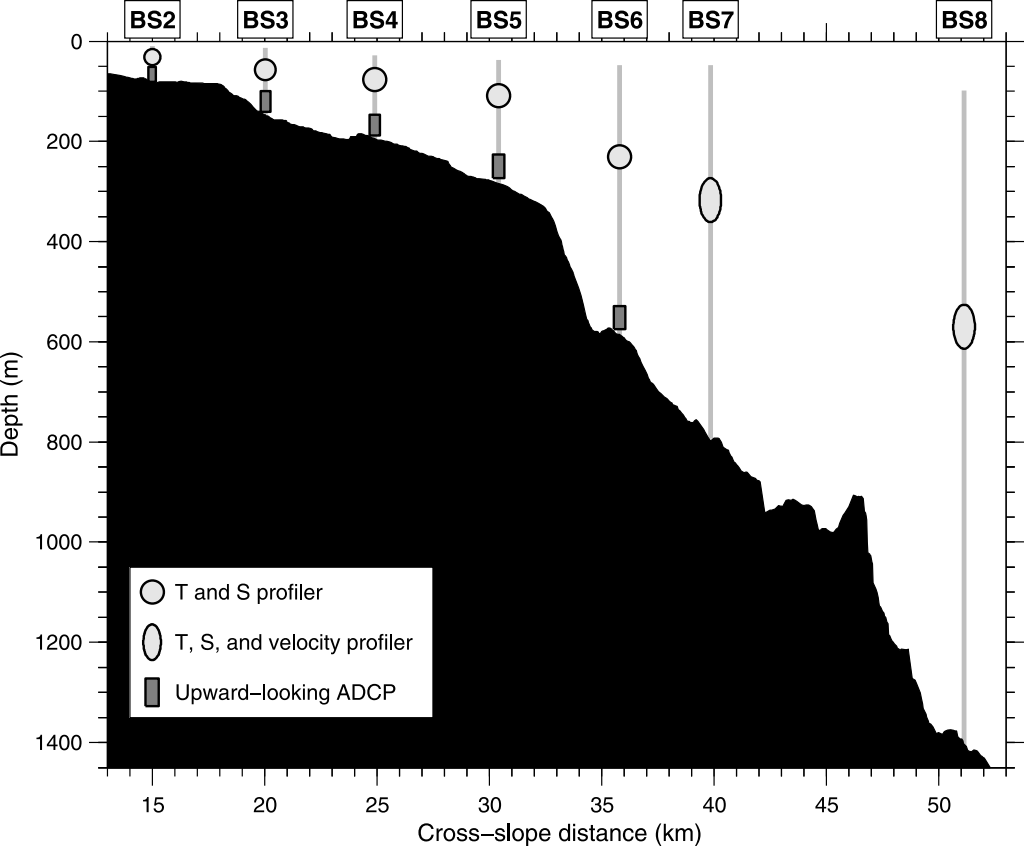
BS2
BS3
BS4
BS5
BS6
BS7
BS8
0
200
400
600
800
1000
1200
1400
Depth (m)
T and S profiler
T, S, and velocity profiler
Upward−looking ADCP
15
20
25
30
35
40
45
50
Cross−slope distance (km)

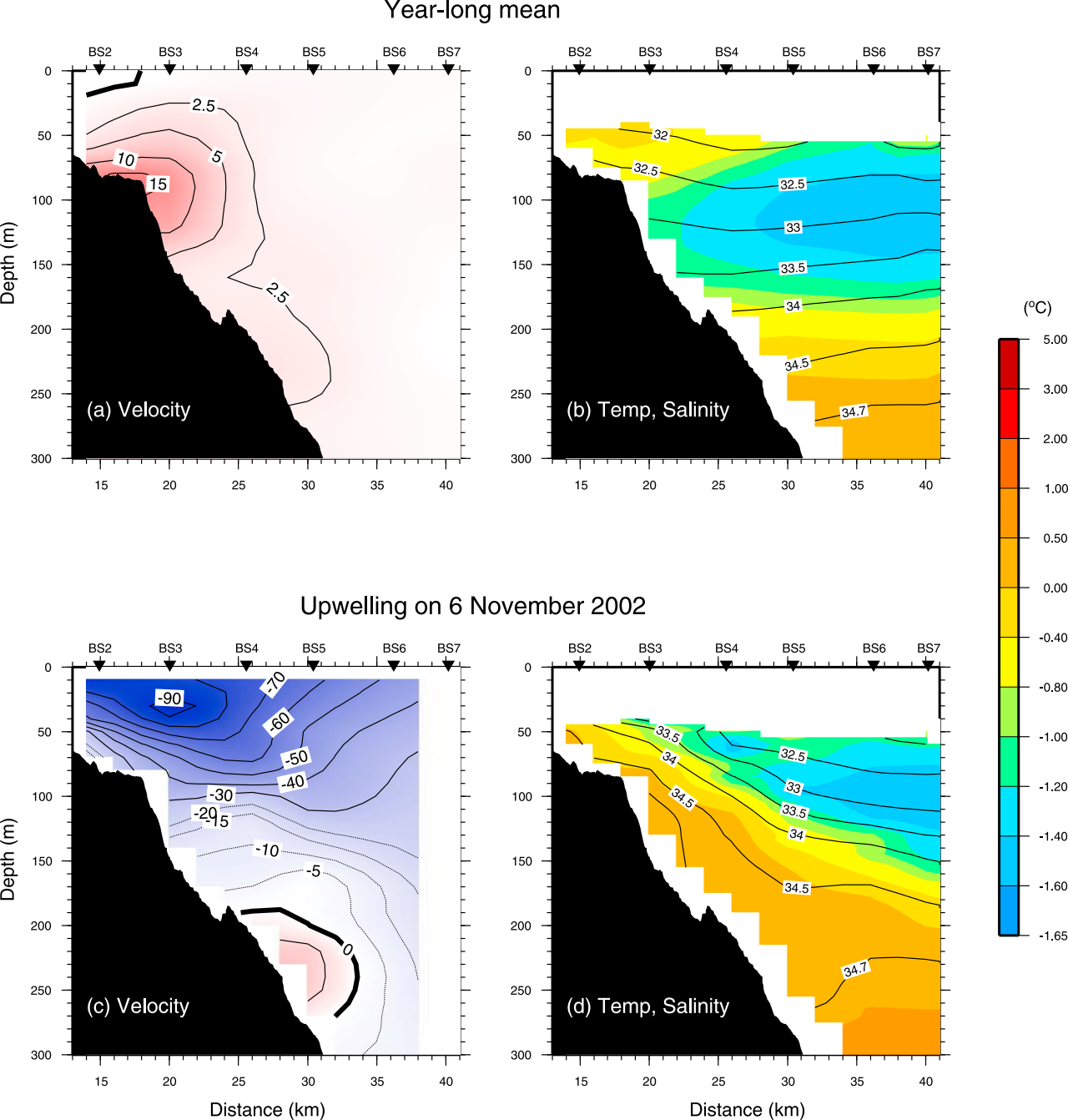
Year-long mean
BS2
BS3
BS4
BS5
BS6
BS7
Depth (m)
(a) Velocity
(b) Temp, Salinity
(°C)
Upwelling on 6 November 2002
(c) Velocity
(d) Temp, Salinity
Distance (km)

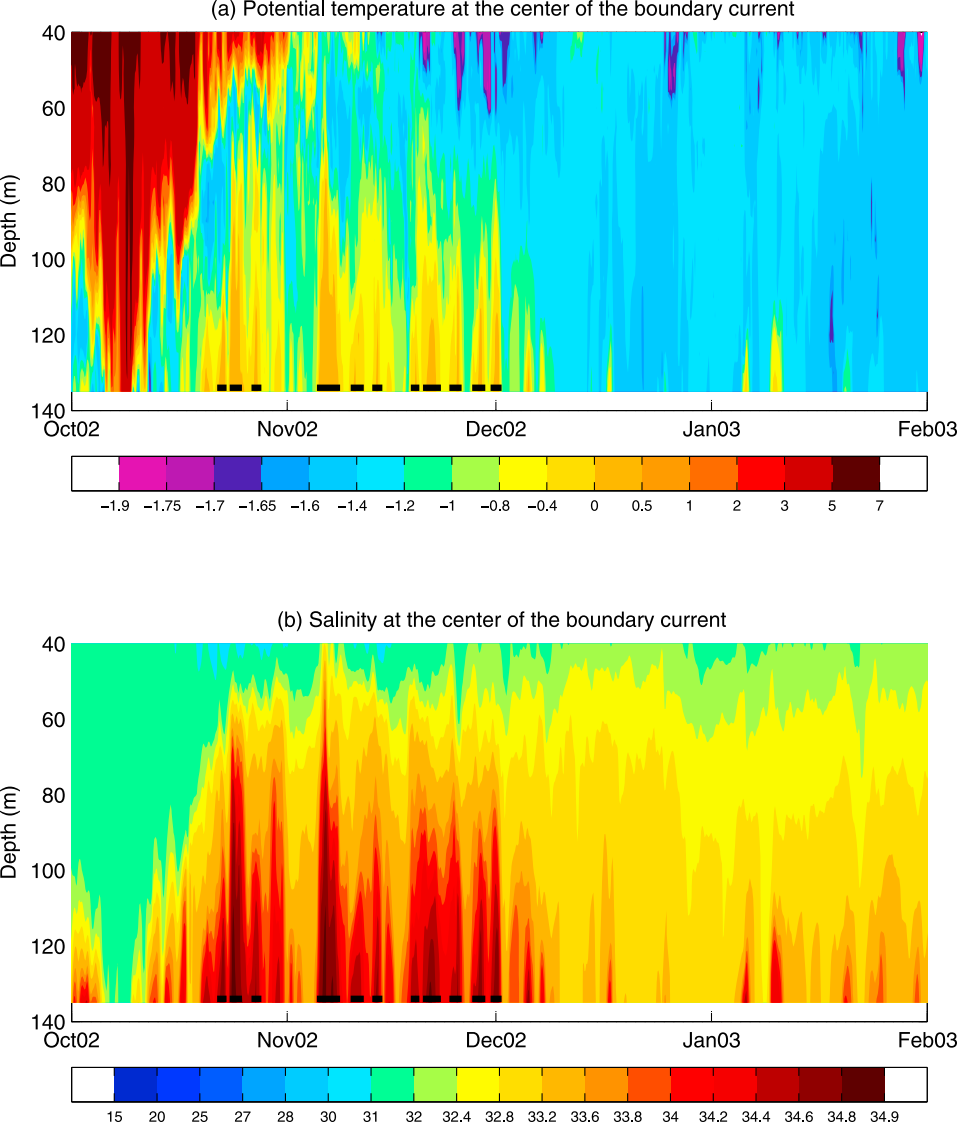
(a) Potential temperature at the center of the boundary current
Depth (m)
40
60
80
100
120
140
Oct02
Nov02
Dec02
Jan03
Feb03
−1.9 −1.75 −1.7 −1.65 −1.6 −1.4 −1.2 −1 −0.8 −0.4 0 0.5 1 2 3 5 7
(b) Salinity at the center of the boundary current
Depth (m)
40
60
80
100
120
140
Oct02
Nov02
Dec02
Jan03
Feb03
15 20 25 27 28 30 31 32 32.4 32.8 33.2 33.6 33.8 34 34.2 34.4 34.6 34.8 34.9

Storm tracks

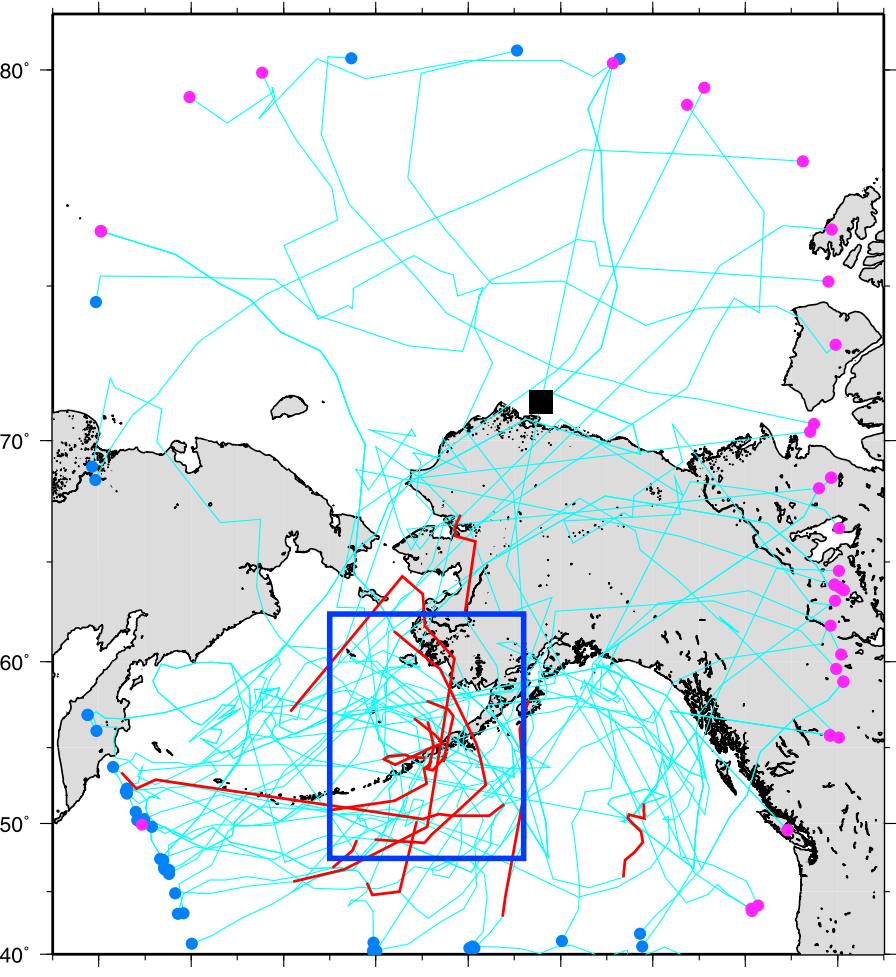

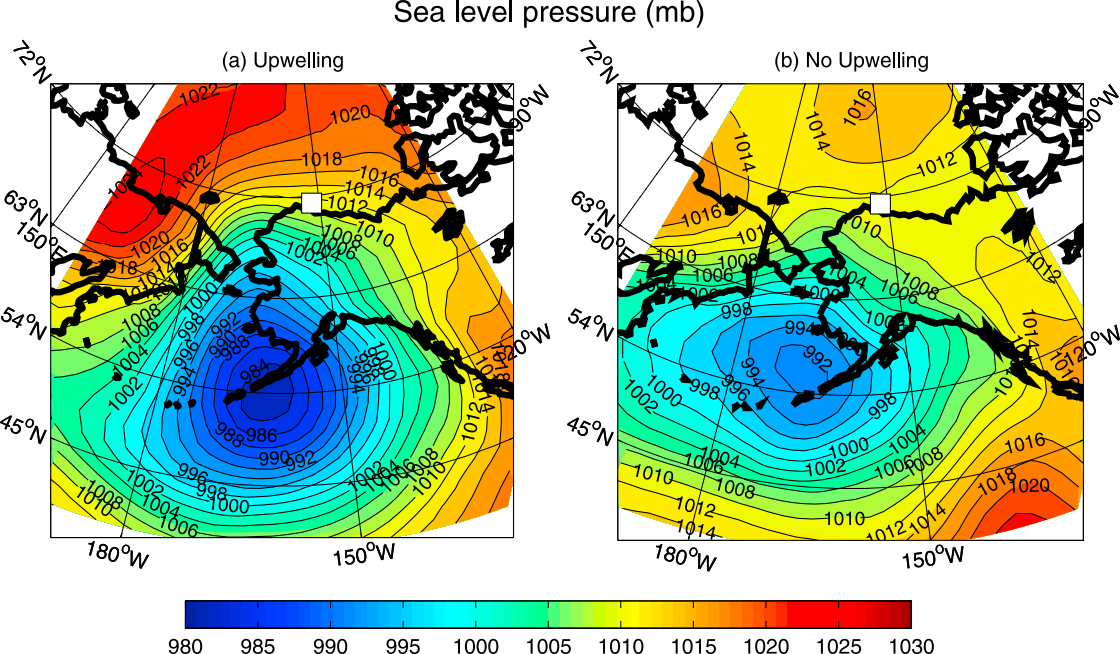
Sea level pressure (mb)
(a) Upwelling
(b) No Upwelling
72°N
63°N
54°N
45°N
150°E
90°W
120°W
180°W
150°W
980
985
990
995
1000
1005
1010
1015
1020
1025
1030

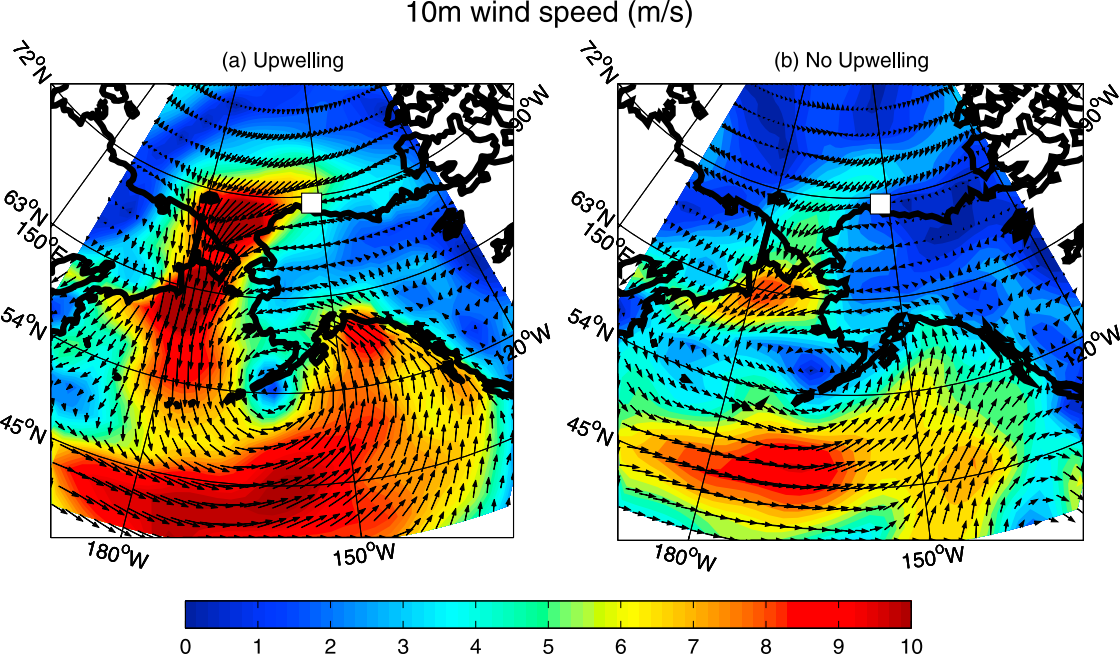
10m wind speed (m/s)
(a) Upwelling
(b) No Upwelling
72°N
63°N
54°N
45°N
150°E
90°W
120°W
180°W
150°W
0
1
2
3
4
5
6
7
8
9
10

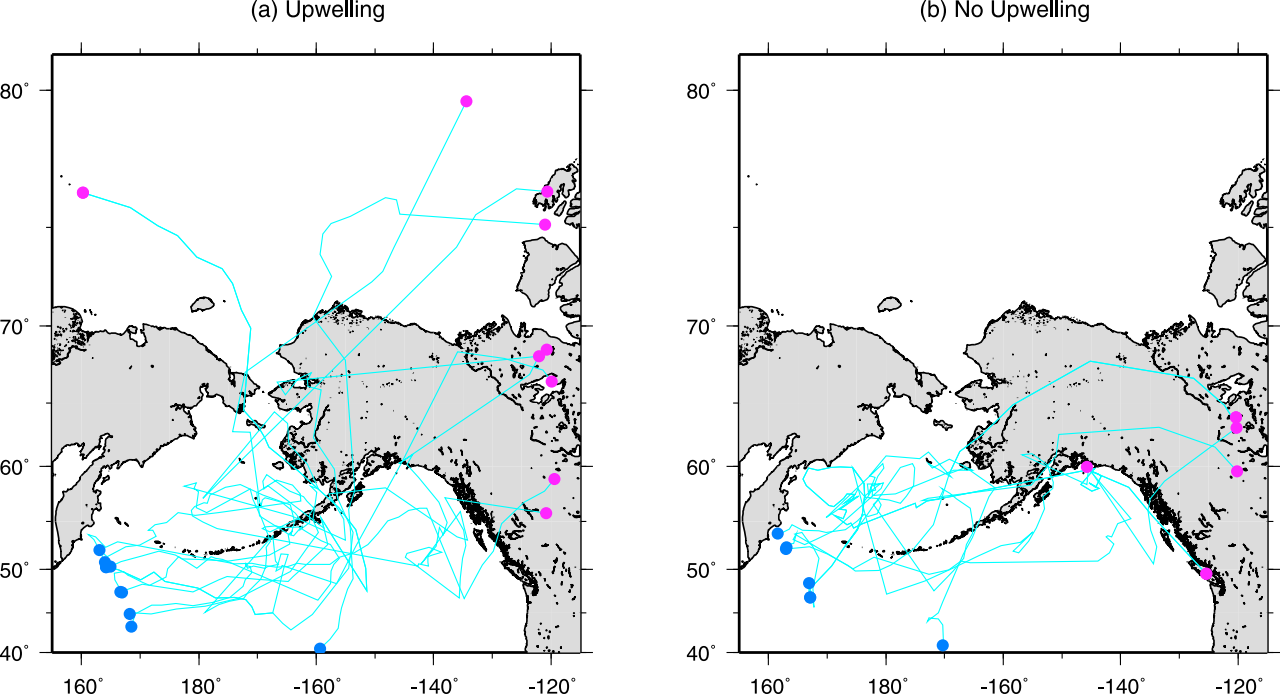
(a) Upwelling
(b) No Upwelling
80°
70°
60°
50°
40°
160°
180°
-160°
-140°
-120°

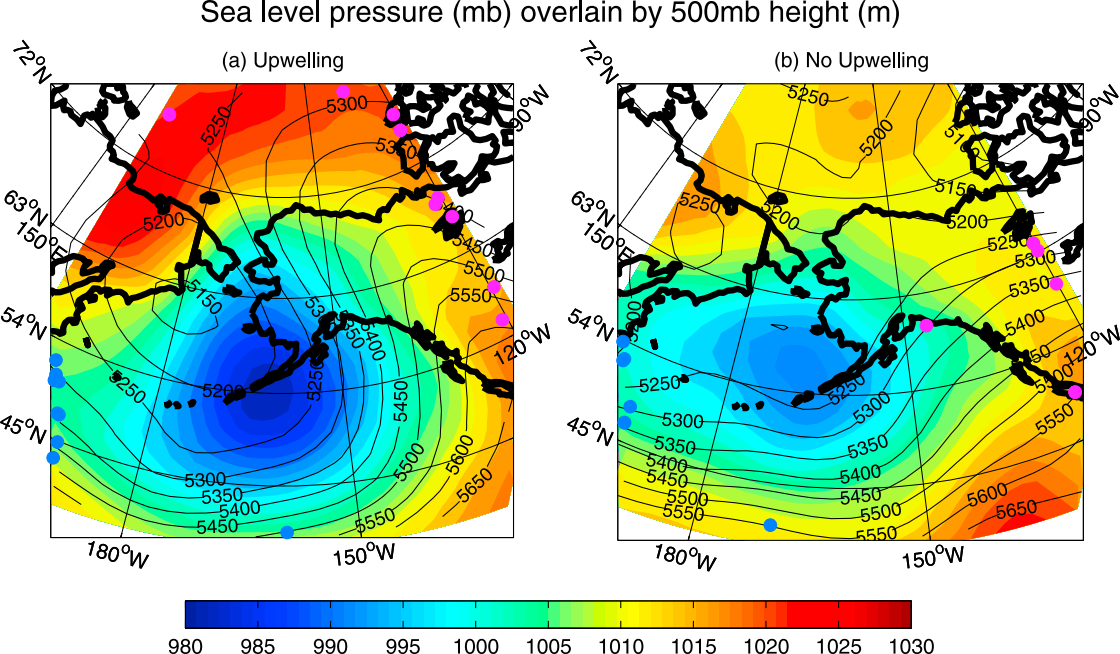
Sea level pressure (mb) overlain by 500mb height (m)
(a) Upwelling
(b) No Upwelling
72°N
63°N
54°N
45°N
150°E
90°W
120°W
180°W
150°W
980
985
990
995
1000
1005
1010
1015
1020
1025
1030

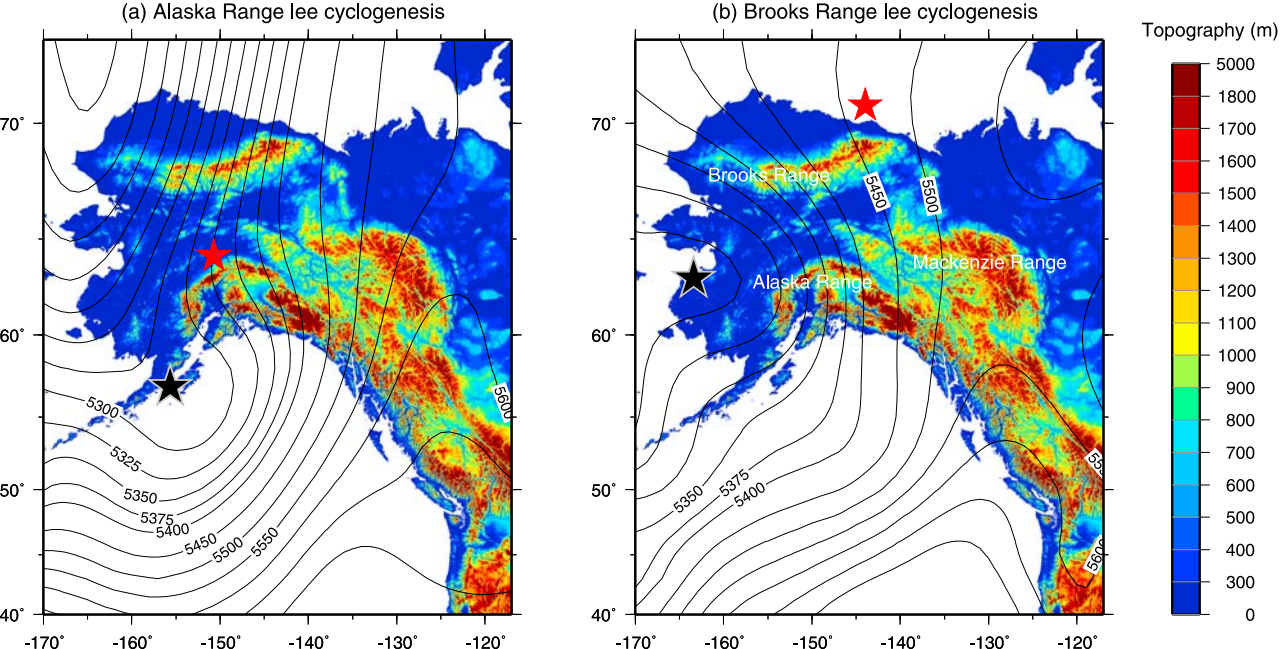
(a) Alaska Range lee cyclogenesis
(b) Brooks Range lee cyclogenesis
Topography (m)
5000
1800
1700
1600
1500
1400
1300
1200
1100
1000
900
800
700
600
500
400
300
0
Brooks Range
Alaska Range
Mackenzie Range
5300
5325
5350
5375
5400
5450
5500
5550
5600
5450
5500
5350
5375
5400
70°
60°
50°
40°
-170°
-160°
-150°
-140°
-130°
-120°

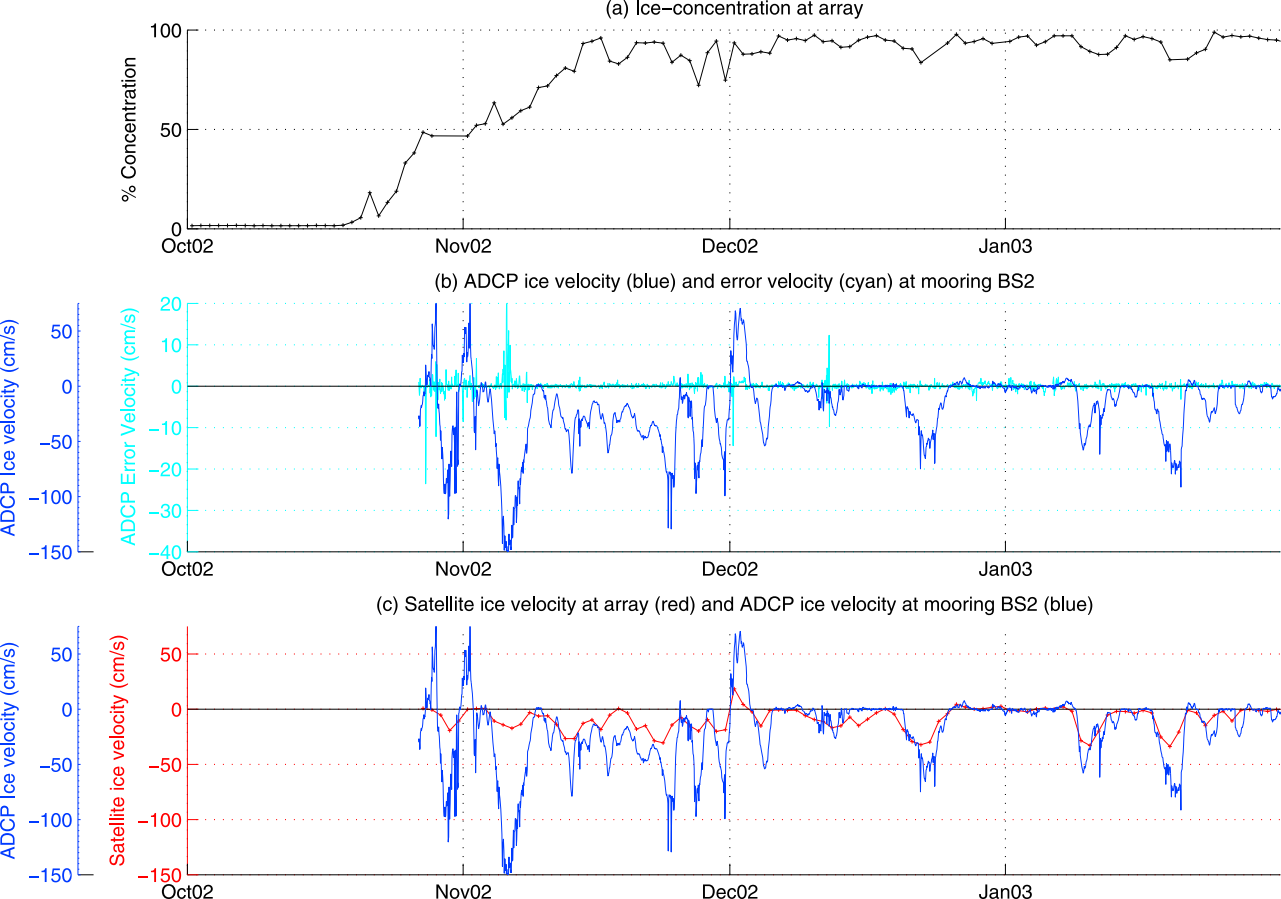
(a) Ice−concentration at array
% Concentration
100
50
0
Oct02
Nov02
Dec02
Jan03
(b) ADCP ice velocity (blue) and error velocity (cyan) at mooring BS2
ADCP Ice velocity (cm/s)
ADCP Error Velocity (cm/s)
50
0
−50
−100
−150
20
10
0
−10
−20
−30
−40
Oct02
Nov02
Dec02
Jan03
(c) Satellite ice velocity at array (red) and ADCP ice velocity at mooring BS2 (blue)
ADCP Ice velocity (cm/s)
Satellite ice velocity (cm/s)
50
0
−50
−100
−150
Oct02
Nov02
Dec02
Jan03

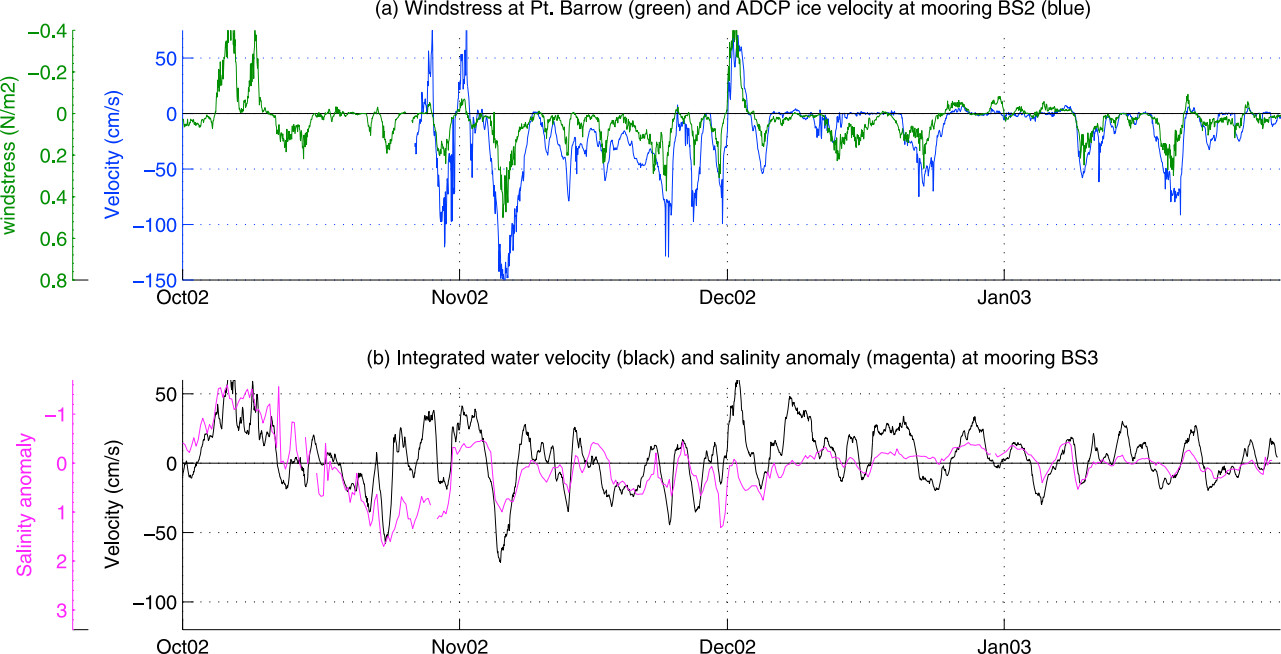
(a) Windstress at Pt. Barrow (green) and ADCP ice velocity at mooring BS2 (blue)
windstress (N/m2)
−0.4
−0.2
0
0.2
0.4
0.6
0.8
Velocity (cm/s)
50
0
−50
−100
−150
Oct02
Nov02
Dec02
Jan03
(b) Integrated water velocity (black) and salinity anomaly (magenta) at mooring BS3
Salinity anomaly
−1
0
1
2
3
Velocity (cm/s)
50
0
−50
−100
Oct02
Nov02
Dec02
Jan03

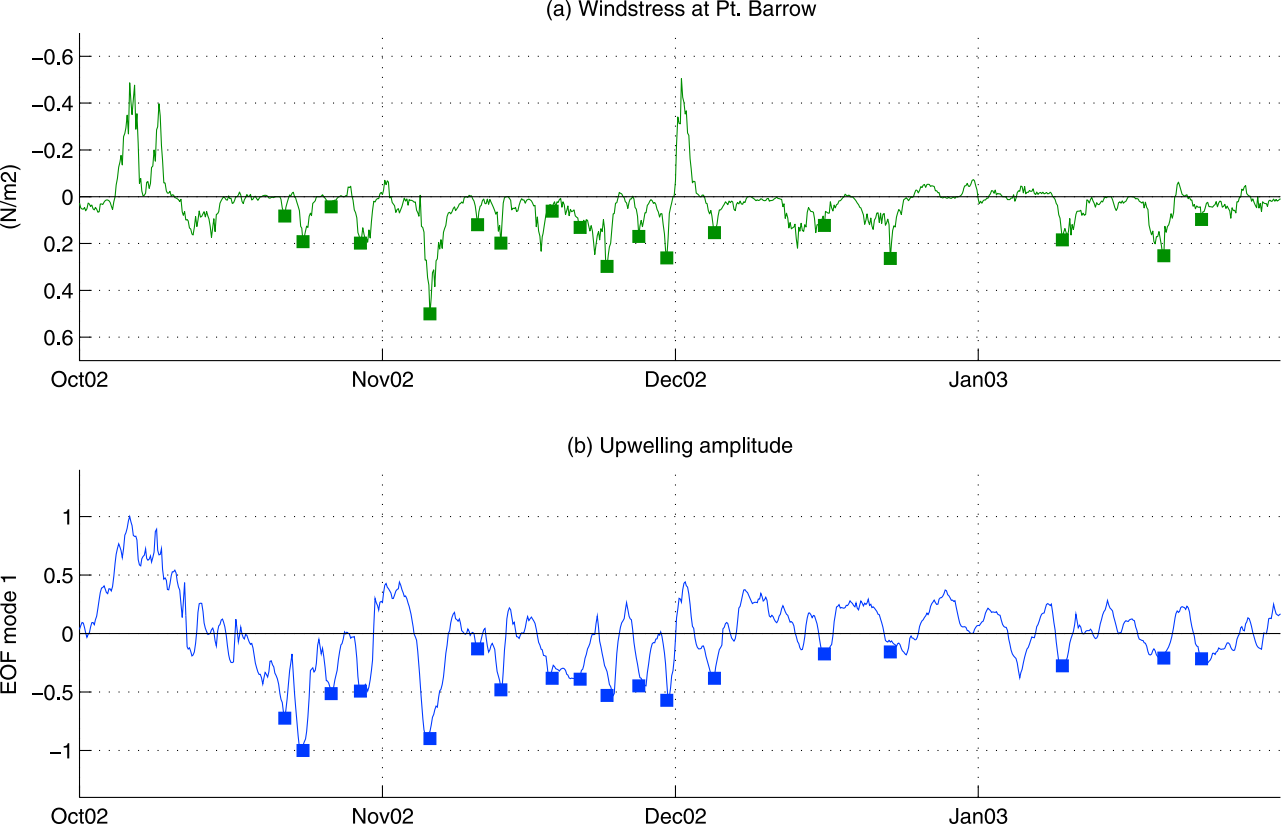
(a) Windstress at Pt. Barrow
(N/m2)
−0.6
−0.4
−0.2
0
0.2
0.4
0.6
Oct02
Nov02
Dec02
Jan03
(b) Upwelling amplitude
EOF mode 1
1
0.5
0
−0.5
−1
Oct02
Nov02
Dec02
Jan03

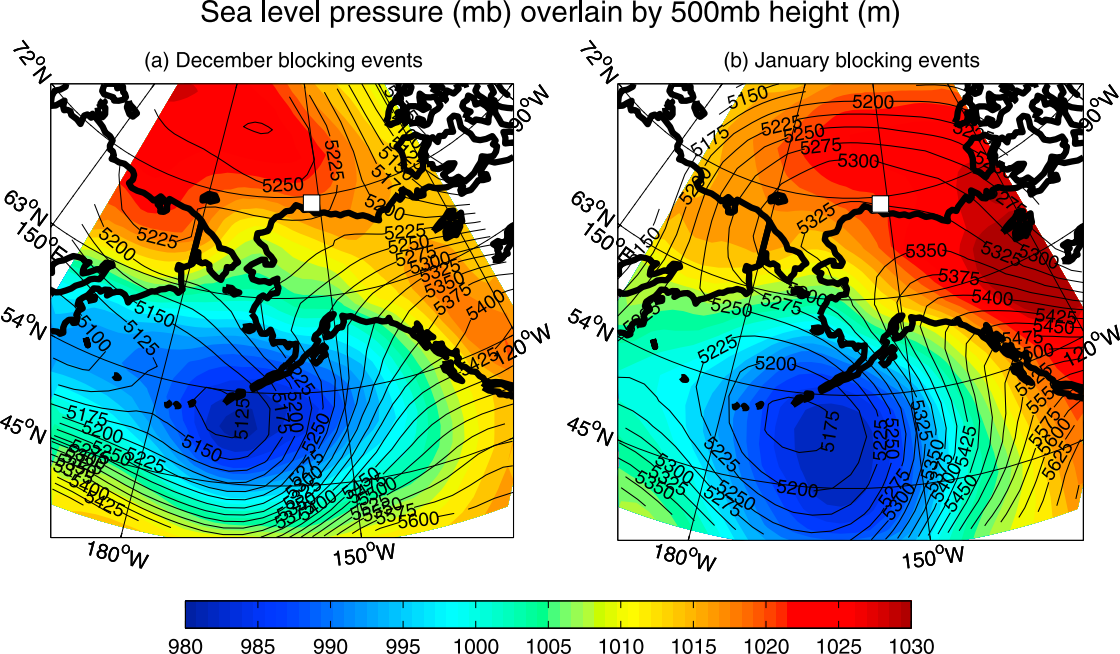
Sea level pressure (mb) overlain by 500mb height (m)
(a) December blocking events
(b) January blocking events
72°N
63°N
54°N
45°N
150°E
90°W
120°W
180°W
150°W
980
985
990
995
1000
1005
1010
1015
1020
1025
1030